5-2018

Extraction and Analysis of Vector Flow Imaging Data in a Pediatric Population

Bailey Stinnett

Extraction and Analysis of Vector Flow Imaging Data in a Pediatric Population

A thesis submitted in partial fulfillment
of the requirements for the degree of
Bachelors of Science in Biomedical Engineering

By: Bailey Stinnett

May 2018
University of Arkansas

TABLE OF CONTENTS

Page

Abstract

Vector flow imaging (VFI) is a new ultrasound technology that provides real time, *angle-independent* visualization of flow velocities in the heart and great vessels. Thus far, VFI has been used for superficial applications due to the limited penetration depth of available transducer probes; however, this depth in smaller pediatric patients enables adequate aortic views. In this project, VFI was used to study pediatric aortic stenosis (PAS)—a congenital heart defect that results in the narrowing of the aorta and/or aortic valve. The decision to refer PAS patients for surgical or catheter-based intervention is initially based on Doppler ultrasound. VFI is potentially more precise, and avoids many of the pitfalls of conventional Doppler ultrasound, namely in the under- or overestimation of pressure differences in the aorta leading to less than ideal treatment timelines. Our goal was to create a method for quantitatively analyzing vectors produced by the VFI machine and to validate VFI technology by attaching an aortic arch phantom to a customized flow loop. This research will set the foundation for the creation of patient-specific aortic arch phantoms.

Introduction

Vector flow imaging (VFI) is a new ultrasound technology that provides real time, *angle-independent* visualization of flow velocities in the heart and great vessels (1). VFI uses transverse oscillation (TO) to view both transverse and axial velocity components simultaneously. Conventional ultrasound technology is limited in that it provides *angle-dependent* visualization of velocity flow along the axis of the ultrasound beam (2). In **Figure 1**, the ultrasound beam is transmitted across the z-axis, but only one velocity component along the axis, v_z, can be estimated; TO overcomes the limitations of conventional ultrasound by enhancing the flow field in the axial and transverse directions, v_x and v_z, respectively. VFI provides greater and potentially more precise velocity flow information for vessels that are oriented nearly parallel to the skin surface. TO has been validated *in vivo* against cardiac magnetic resonance (CMR) angiography (3,4) and conventional spectral Doppler ultrasound (5, 6).

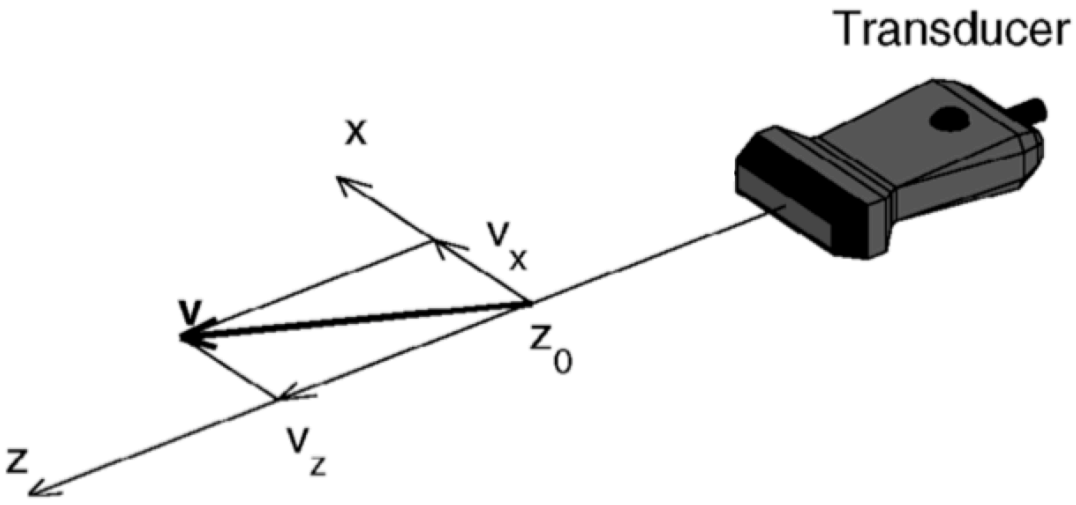

Figure 1: A conventional ultrasound system estimates only the axial velocity component, v_z, situated at a depth of z_0 and moving with velocity vector v. The TO method estimates both v_x and v_z. Adapted from (2).

Thus far, VFI ultrasound imaging has been used in applications where the vessel of interest is superficial, such as the carotid artery (7), arteriovenous fistula for hemodialysis (8), or the femoral vein (9). However, pertinent information about cardiac flow has been recognized in intraoperative imaging; in these tests, VFI data is acquired directly from the heart via an epicardial transducer (1). The penetration depth of commercially available VFI transducers has been previously estimated at 5 cm, which has discouraged its use in transthoracic cardiac applications; however, this limited depth enables adequate aortic views in smaller pediatric patients.

In this project, VFI was used to study pediatric aortic stenosis (PAS)—a congenital heart defect that results in the narrowing of the aorta and/or the aortic valve. This condition comprises 3-6% of all congenital heart defects and treatment is required. The decision to refer PAS patients for surgical or catheter-based intervention is initially based on Doppler ultrasound (10). To minimize risks associated with invasive procedures, and to avoid multiple re-operations, it's best to intervene as late as possible, but early enough to preserve myocardial function in the long-term.

The decision to intervene on a stenotic aortic valve is based on the pressure differences across the valve. Currently, cardiac catheterization is the gold standard for pressure measurement, but this method requires the placement of invasive manometers in the child's heart (11). This technique is highly impractical to perform namely, because it requires general anesthesia, multiple highly trained personnel, contrast agents, and carries the risks associated with an invasive procedure. CMR imaging is suggested as an alternative, but it shares many of the same pitfalls with cardiac catheterization: multiple highly trained personnel are required to operate the magnet and software, most children require general anesthesia to remain still for a

study that frequently lasts longer than 30 minutes, and contrast agents are injected into the patient (12).

Given the downsides of catheterization and CMR, ultrasound is routinely used to noninvasively predict the pressure difference across a valve, with reasonable, although imperfect accuracy. Thus, there is a pressing need for accurate, comprehensive, non-invasive, non-contrast imaging to better treat this patient population. The two methods of interest for estimating the pressure differences across the aorta include the simplified Bernoulli's equation and a fluid-structure interaction (FSI) model (**Figure 2**).

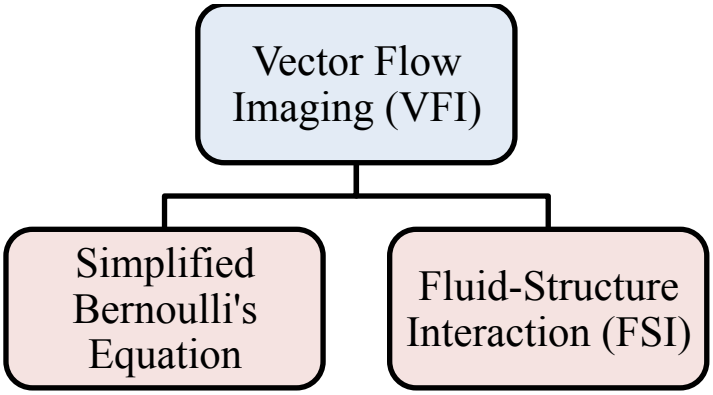

Figure 2: Flowchart of the two methods that will be used as estimated comparisons of the pressure drop across the aorta and/or aortic valve.

In echocardiography, the simplified Bernoulli's equation is used to approximate the pressure difference. This equation states that:

$$\Delta P = 4V^2$$

where ΔP is the change in pressure across the valve and V is the highest velocity as measured by ultrasound (13). It is generally accepted that the mean pressure difference across the aortic valve

as measured by the simplified Bernoulli's equation best approximates the catheter-based "peak to peak" pressure drop, which is the difference between the peak pressure in the left ventricle and the peak pressure in the aorta (10). While the simplified Bernoulli equation assists in approximating the pressures, multiple assumptions are made; these include: the angle of interrogation is adequate to detect the highest velocity, the velocity proximal to the valve is negligible, and there is no significant resistance. Since ultrasound-based measurements can either underestimate or overestimate pressure differences, children may receive treatment earlier or later than would otherwise be ideal.

The second method, FSI modeling, studies the flow of blood through a flexible structure such as the aorta or aortic valve. Previous geometrical models in FSI have been used to compute pressure and/or velocity values across the aorta (14). This form of computational modeling can be used to create patient-specific models (14, 15); this method will enable us to validate the VFI method through the pressure prediction across a patient-specific stenotic aorta. After using the simplified Bernoulli's equation, and determining the inlet and outlet pressures across the aorta, a FSI model from an external source will be applied to the VFI files for comparison of the pressure drop across the aorta and/or aortic valve.

Aortic replicas called "phantoms" are routinely used in research to mimic patient specific cardiovascular functions *in vitro*. These phantoms study the shape and mechanical behavior of a patient's vessel and can provide validation for imaging techniques (16). For the purposes of this study, two aortic arch phantoms were created for the *in vitro* analysis of pressure drop across the aorta or aortic valve. The first phantom was made out of silicone and the second phantom was made out of Ballistics gel. The phantom creation is proprietary, so no details can be revealed.

The presence of air bubbles in the phantom affects the accuracy of the VFI transducer when measuring pressure.

Based off a similar flow loop design in *Pasta et al.*, a flow loop schematic shown in **Figure 3** was designed to measure the pressure differential across the aortic arch phantom. Two pressure transducers will be inserted into the aortic phantom and a pulsatile pump will be used to generate fluid flow across the aortic arch.

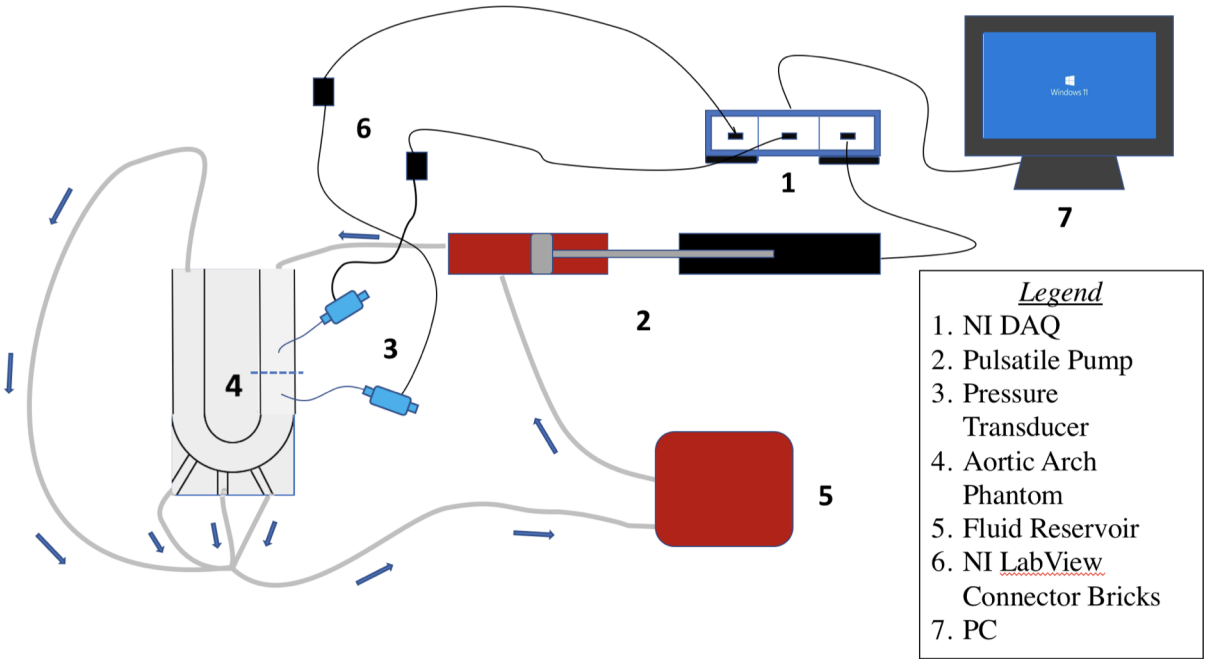

Figure 3: Schematic of aortic arch phantom flow loop

The Division of Cardiology at Arkansas Children's Hospital (ACH) and Arkansas Children's Research Institute (ACRI) purchased a VFI system for this study; however, the machine outputs video files with vectors, but physicians have no way to quantitatively analyze these vectors. Therefore, the first goal was to develop a method for quantitatively analyzing the VFI data and the second goal was to develop an aortic arch phantom that could be used as an *in vitro* model to study pressure differences across the aortic valve of a PAS patient. The overall

objective of this study was to validate the VFI method by attaching an aortic arch phantom to a cardiac flow loop to obtain pressure measurements.

Materials and Methods

Obtainment of VFI Data

VFI video data from 9 patients (8 healthy and 1 diseased) have been provided by ACH and ACRI for analysis of vector data. These raw videos ranged in length from 1 second to 25 seconds and all were formatted as .avi files. Data collection is still ongoing at this time. A VLC media player was used to view each .avi file. Upon receiving the data, the files were cropped to include the length of time for one heart cycle. Once cropped, a coding algorithm developed by a University of Arkansas Computer Science and Computer Engineering (UA CSCE) senior capstone group was applied to the color wheel of each .avi file to obtain numerical vector information from the hue-saturation luminance (HSL) values of each color in the image. In this algorithm, only the colored pixels that corresponded to the color wheel in the image were considered; therefore, the black and white pixels were excluded from analysis. The vector information obtained from the patient files include vector data in .csv format that corresponded to the spatial position, location, and speed (in cm/s) of the pixels in each frame of the VFI file. Each .csv file contained data from individual frames taken within each image.

Idealized Aortic Arch

The arch design was based off of healthy arch data and serves as a precursor to patient-specific diseased phantoms (16, 17,18). The same arch design was used in both the silicone and gel phantoms, however, the length of the ascending aorta was extended to match the length of the

descending aorta in the gel phantom to allow for better placement of the arch within the SolidWorks box. The idealized healthy aortic arch was designed in SolidWorks. The outer diameters of the ascending and descending aorta were 12.70 mm and 15 mm, respectively. On the top of the arch, the outer diameters of the brachiocephalic trunk, left common carotid artery, and left subclavian artery, were 15.41 mm, 4.70 mm, and 19.34 mm, respectively. The idealized arch was 140 mm in length.

Silicone Phantom

A rectangular shaped box with a small cutout was designed in SolidWorks to create the silicone arch mold. This box consisted of an acrylic base with 6 acrylic separate edge/side pieces, fitting the ascending aorta, descending aorta, and the brachiocephalic trunk, left common carotid artery, and left subclavian artery. The completed arch box for the silicone phantom measured 180 mm by 2.78 mm by 120.11 mm; the width of 2.78 mm corresponded to the sidepiece with the three holes for the brachiocephalic trunk, left common carotid artery, and left subclavian artery. The acrylic box components were cut using a laser cutter.

After constructing the box, a silicone mixture was prepared. The silicone and catalyst were measured by weight by a ratio of 10 to 1. After measuring, the catalyst was added to the silicone container and gently mixed to limit the formation of air bubbles. Once thoroughly mixed, the container was placed in a vacuum twice for ten minutes. Upon completion of the second ten minutes, the silicone was taken out of the vacuum chamber and slowly poured from the mixing container into the acrylic box at an elevated height. After the silicone mixture was poured, the acrylic box was placed in the vacuum twice for 6 additional minutes each time. During this degassing process, the silicone slowly rises by climbing up the walls of the container,

so after each vacuuming step, 2-3 minutes were taken to allow the air bubbles to collapse back down to the initial silicone level. After the final vacuuming step, the acrylic box was removed from the vacuum chamber, covered, and set aside for 24 hours to allow time for the phantom to cure. Once cured, the silicone phantom was removed from the acrylic box.

Gel Phantom

While the silicone phantom and the ballistics gel phantom are similar, there were slight differences in how each phantom was made, specifically in regard to the arch box and material. For the gel phantom, an arch box consisting of three individual components—the rectangular box base with two rectangular long-edge sidepieces attached and two shorter individual end pieces—were designed in SolidWorks. A sheet of stainless steel was used to create the base and sides (*A* and *B)* of the box shown in **Figure 4**, while a MakerBot 3D printer with red and white ABS (acrylonitrile butadiene styrene) filament was used to print the two end pieces of the box. With all three of the box pieces attached, the completed gel arch box **(Figure 4)** measured 109 mm by 84 mm by 80 mm.

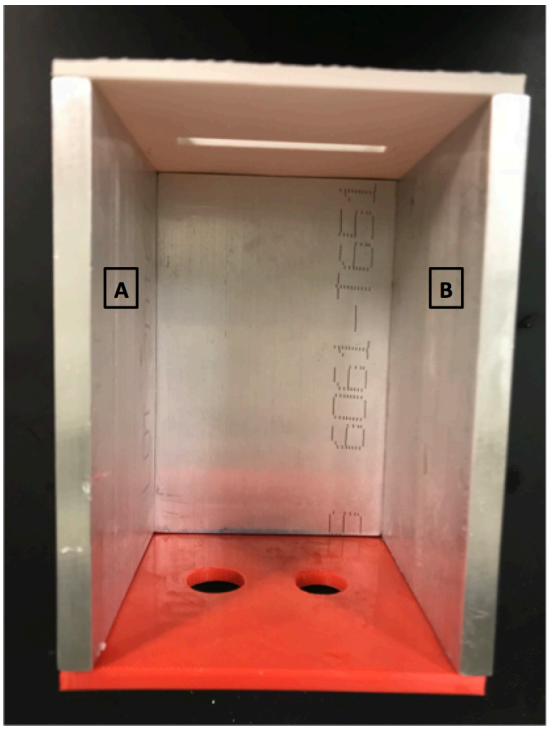

Figure 4: Gel phantom box without the arch. A and B correspond to the sides of the base.

A large section of ballistics gel was broken into fragments and placed into a metal container. The container was baked in an oven at 275˚F for 3 hours. After 3 hours, the gel was removed from the oven and put into a vacuum chamber for 6 minutes. Once finished, the gel was baked for another 20 minutes. While the gel reheated, an ice bath was prepared. The three box pieces were placed in the freezer to limit bubble formation once the gel was poured into the arch box. After 20 minutes, the gel was removed from the oven and placed into the vacuum for an additional 6 minutes. After degassing, the gel was placed back in the oven for 20 minutes. While the gel reheated, the arch box was removed from the freezer and a releasing agent was applied on all parts of the box exposed to the gel. To limit bubble formation in the gel, the clamped arch box was placed in the refrigerator for 20 minutes. After this time, the box was removed from the refrigerator and a heat gun was applied on the exposed surface of the gel. The

heat gun assisted in removing air bubbles near the surface of the gel. After 24 hours, a heat gun was applied to the exposed surface of the gel once again. After an additional 24 hours, the gel phantom was removed from the arch box.

Results

The patient files provided by ACH and ACRI contained echocardiographic views of patient aortas and/or aortic valves with and without vectors. Of the provided VFI files, the parasternal long-axis view (**Figure 5**) provided the greatest clarity for visualization of anatomical features in the pediatric patients.

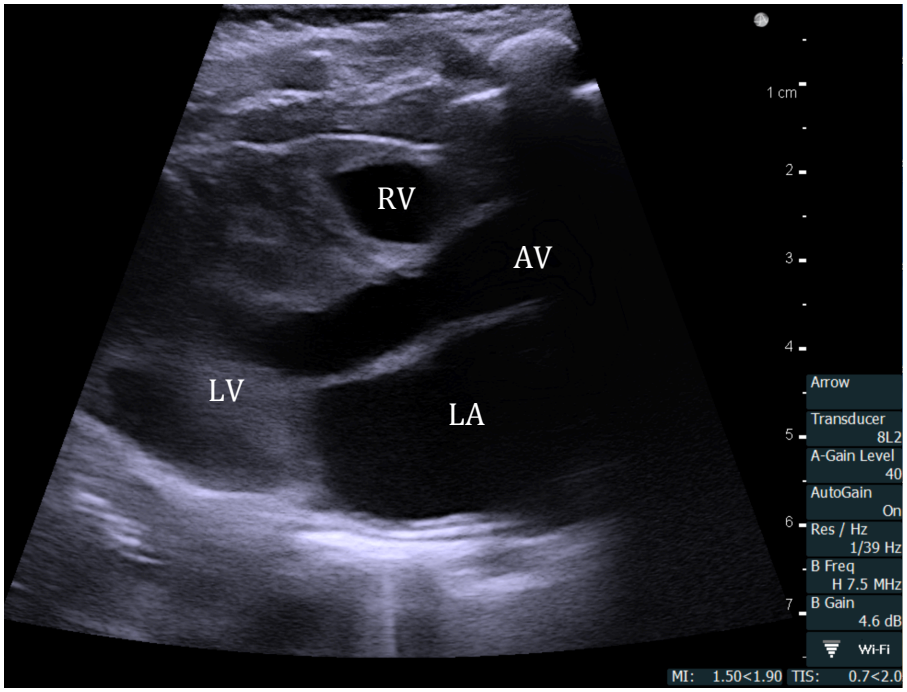

Figure 5: VFI echocardiographic parasternal long-axis view of a stenotic pediatric aorta without vectors. RV = right ventricle, LA = left atrium, LV = left ventricle, AV = aortic valve

With the addition of vectors on the VFI echocardiogram (**Figure 6**), we were able to qualitatively visualize the vector flow velocities in the heart using the color wheel. Red and pink pixel colors were largely associated in the location of the open aortic valve. In the VFI echocardiogram of the healthy patient, the vectors were distributed in a fairly uniform manner. The colored pixels of the velocity flow shifted to neighboring colors represented in the color wheel.

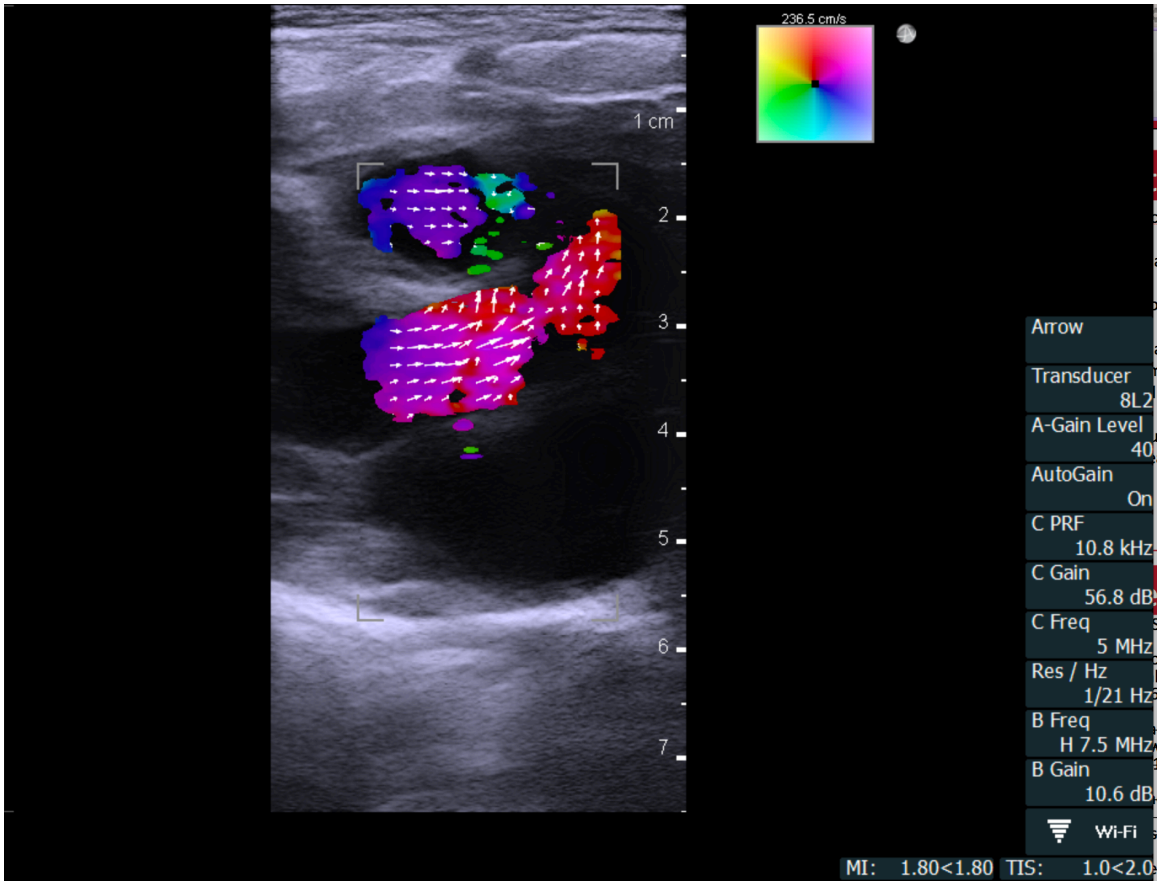

Figure 6: VFI echocardiographic parasternal long-axis view of a healthy pediatric aorta with the addition of vectors.

In the VFI echocardiogram of the diseased patient (**Figure 7**), there was a noticeable difference in the vector velocities or pixel color across the open aortic valve. While some of the

open aortic valve had red pixels, there were a multitude of other colors represented across the color wheel gradient. The vectors were not distributed in a uniform manner, specifically, the vectors pointed in multiple directions and varied greatly in length.

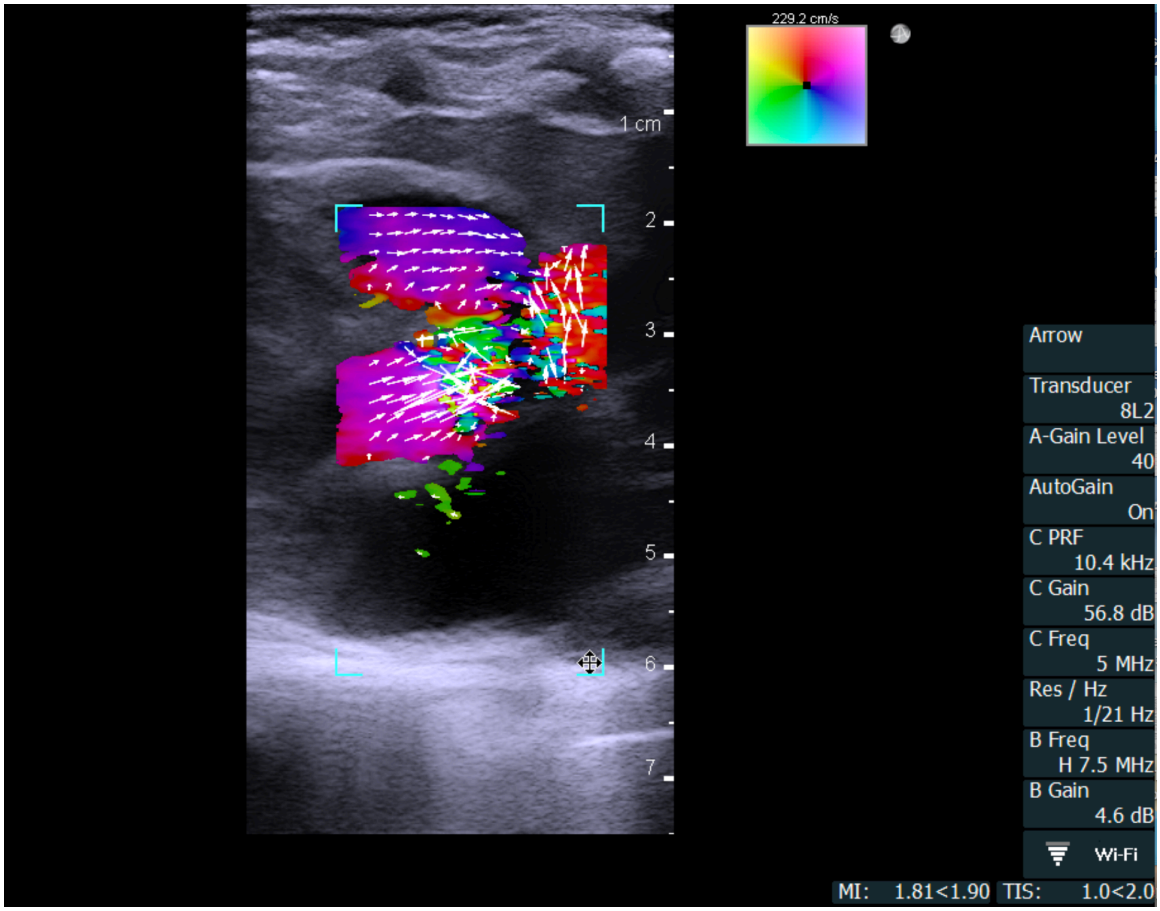

Figure 7: VFI echocardiographic parasternal long axis view of stenotic aorta.

Once the coding algorithm was applied to the cropped VFI file, a .csv file **(Figure 8)** was generated with 14 individual sheets corresponding to the 14 frames in the cropped video. The *X* and *Y* variables corresponded to the overall pixel location, *Vx* and *Vy* corresponded to the spatial positioning, and speed corresponded to the vector velocity in centimeters per second. This result

confirmed that quantitative vector information can be obtained from the VFI files. The generated .csv file will be used in the simplified Bernoulli's equation and then in the FSI model.

Frame Index	Vector Index	X	Y	Vx	Vy	Speed (cm/s)
0	0	450	34	74.81	-35.21	82.68
0	1	496	34	88.02	-48.41	100.45
0	2	541	34	74.81	-52.81	91.57
0	3	547	34	79.21	-44.01	90.62
0	4	279	35	88.02	-48.41	100.45

Figure 8: Example of vector output data generated from .avi files.

The next step will be to find the maximum velocities in each of the frame files. Once these 14 maximum velocities are found from the 14 individual sheets, the maximum velocity from the acquired maximum velocities will be found. This velocity provides the overall maximum velocity, V, across the cardiac cycle. The pressure drop across the aortic valve will be calculated by plugging in the maximum velocity, V, into the simplified Bernoulli's equation. The estimated pressure drop will then be compared to the pressure drop found in the FSI model and the pressure drop from an invasive technique such as catheterization and/or CMR.

An idealized aortic arch design was used in the gel phantom to model a healthy aortic arch. The arch was hollow to allow for the movement of fluid through the arch when dissolving the arch. In this prototype, the ascending aorta was extended to equal the length of the descending aorta for better placement and securement of the arch in the box. In this design, the extended ascending aorta of the healthy arch should not affect the pressure transducer measurements, since the pressures should be theoretically close in value across the arch. The

healthy arch design will serve as a foundation for future SolidWorks designs of physiologically accurate patient-specific arches for PAS patients.

The completed silicone phantom closely resembled a human arch. The decision was made to switch the phantom material from silicone to Ballistics gel. The gel is similar to silicone, but is more flexible to better resemble a human aorta; additionally, in the creation of other cardiovascular phantoms in lab, it was noted that the gel produced fewer air bubbles throughout the phantom compared to the silicone.

With the attachment of our customized flow loop, the pressure differences within the aortic model can be obtained. The process for the creation of the healthy phantom will be used in the creation of patient-specific phantoms. While the gel phantom is not flawless, namely in the formation of air bubbles, we now have a foundation set for the creation of future gel phantoms.

Discussion and Future Direction

There was an indication of increased turbulence across the aortic valve of the PAS patient (**Figure 7**) due to the broad spectrum of colored pixels and disorder among the vector velocities. This study confirmed that numerical vector data could be successfully extracted from the patient VFI files provided by ACH and ACRI (**Figure 8**). While the .csv files provided pixel locations, we have not yet determined which specific pixel locations correspond to the inlet and outlet information. The next step will be the specification of inlet and outlet locations on the aorta; once these inlets and outlets are defined, we will then be able to insert the vector data into a fluid-structure interaction (FSI) model for further estimations of aortic pressure.

The silicone phantom served as the basis for the creation of the gel phantom. The gel enabled us to more effectively mimic the flexible characteristic of human tissue around the aorta. The transparency of the phantom will allow for clear visualization and placement of pressure transducers within the phantom. Our method of creating the idealized healthy arch and gel phantom will set the foundation for the future development of patient-specific aortic arch phantoms for PAS and further medical applications.

To validate the setup of the flow loop, pressure transducers will be inserted into the arch outline of the gel phantom. After attaching all components of the flow loop, we will be able to validate our pressure transducers by measuring the pressure across the healthy arch. Since the healthy arch has no stenosis, we should theoretically see no pressure drop across the healthy arch, so we expect the pressure measurements to be within a few millimeters of mercury (mmHg) of each other. To further validate our initial flow loop setup, we plan to apply pressure on the sides of the healthy gel phantom to mimic stenosis.

Once the setup is validated, the healthy phantom will be switched on a patient-by-patient basis with a patient-specific phantom to study the pressure differential across a region of stenosis. The location of the pressure transducers within the patient-specific phantom will differ depending on the stenosis of the patient. The attachment of the patient specific aortic arch phantoms to the completed flow loop will allow for the validation of measurements using invasive pressure sensors and particle-imaging velocimetry (PIV).

The use of pressure measurements to decide when to intervene is important in minimizing risks associated with the treatment of PAS. In this novel type of ultrasound technology, further study into the limitations of VFI is needed. The application of VFI

technology will provide a potentially more precise option for predicting pressure drop across the aorta and/or aortic valve in all PAS patients.

Acknowledgements

I would like to thank my research advisors, Dr. Hanna Jensen and Dr. Morten Jensen, for their support and mentorship throughout my time in the Cardiovascular Biomechanics Lab. I am grateful to Megan Laughlin and Jackson Mosley for their assistance and encouragement on this project. I would also like to acknowledge the University of Arkansas Computer Science and Computer Engineering capstone team for development of the VFI coding algorithm. This project was supported by ACRI and UAMS.

References

1. Hansen KL, Moller-Sorensen H, Pedersen MM, Hansen PM, Kjaergaard J, Lund JT, et al. First report on intraoperative vector flow imaging of the heart among patients with healthy and diseased aortic valves. Ultrasonics. 2015;56:243-50.
2. Udesen J, Jensen JA. Investigation of transverse oscillation method. IEEE Transactions on Ultrasonics, Ferroelectrics and Frequency Control 2006;53(5):959–71.
3. Bjaerum S, Torp H, Kristoffersen K. Clutter filter design for ultrasound color flow imaging. IEEE Transactions on Ultrasonics, Ferroelectrics, and Frequency Control. 2002;49(2):204-16.
4. Kruse DE, Ferrara KW. A new high resolution color flow system using an eigendecomposition- based adaptive filter for clutter rejection. IEEE Trans Ultrason Ferroelectr Freq Control. 2002;49(10):1384-99.
5. Lovstakken L, Bjaerum S, Kristoffersen K, Haaverstad R, Torp H. Real-time adaptive clutter rejection filtering in color flow imaging using power method iterations. IEEE Trans Ultrason Ferroelectr Freq Control. 2006;53(9):1597-608.
6. Evans DH, Jensen JA, Nielsen MB. Ultrasonic colour Doppler imaging. Interface Focus. 2011.
7. Udesen J, Nielsen MB, Nielsen KR, Jensen JA. Examples of In Vivo Blood Vector Velocity Estimation. Ultrasound Med Biol. 2007;33(4):541-8.
8. Hansen PM, Olesen JB, Pihl MJ, Lange T, Heerwagen S, Pedersen MM, et al. Volume flow in arteriovenous fistulas using vector velocity ultrasound. Ultrasound Med Biol. 2014;40(11):2707- 14.

9. Hansen PM, Pedersen MM, Hansen KL, Nielsen MB, Jensen JA. Examples of Vector Velocity Imaging. IFMBE Proceedings: Springer; 2011. p. 77-80.
10. Feltes TF, Bacha E, Beekman RH, 3rd, Cheatham JP, Feinstein JA, Gomes AS, et al. Indications for cardiac catheterization and intervention in pediatric cardiac disease: a scientific statement from the American Heart Association. Circulation. 2011;123(22):2607-52.
11. Saikrishnan N, Kumar G, Sawaya FJ, Lerakis S, Yoganathan AP. Accurate assessment of aortic stenosis: a review of diagnostic modalities and hemodynamics. Circulation. 2014;129(2):244-53.
12. Markl M, Schnell S, Wu C, Bollache E, Jarvis K, Barker AJ, et al. Advanced flow MRI: emerging techniques and applications. Clin Radiol. 2016.
13. Goldberg SJ, Allen HD, Sahn DJ. Pediatric and adolescent echocardiography: a handbook: Year Book Medical Publishers; 1980.
14. Crosetto P, Reymond P, Deparis S, Kontaxakis D, Stergiopulos N, Quarteroni A. Fluid–structure interaction simulation of aortic blood flow. Computers & Fluids. 2011;43(1):46–57.
15. Taylor CA, Figueroa CA. Patient-Specific Modeling of Cardiovascular Mechanics. Annual Review of Biomedical Engineering. 2009;11(1):109–34.
16. Pasta S, Scardulla F, Rinaudo A, Raffa GM, D'Ancona G, Pilato M, et al. An In Vitro Phantom Study on the Role of the Bird-Beak Configuration in Endograft Infolding in the Aortic Arch. Journal of Endovascular Therapy. 2016;23(1):172–81.
17. Hütter L, Geoghegan PH, Docherty PD, Lazarjan MS, Clucas D, Jermy M. Fabrication of a compliant phantom of the human aortic arch for use in Particle Image Velocimetry

(PIV) experimentation. Current Directions in Biomedical Engineering. 2016 Jan1;2(1):493–7.

18. Urbina J, Sotelo JA, Springmüller D, Montalba C, Letelier K, Tejos C, et al. Realistic aortic phantom to study hemodynamics using MRI and cardiac catheterization in normal and aortic coarctation conditions: Realistic Thoracic Aortic Phantom. Journal of Magnetic Resonance Imaging. 2016;44(3):683–97.